Non-Fickian diffusion in biosourced materials: Prediction of the delay between relative humidity and moisture content

A. Challansonnex, J. Casalinho, P. Perré

To cite this version:

A. Challansonnex, J. Casalinho, P. Perré. Non-Fickian diffusion in biosourced materials: Prediction of the delay between relative humidity and moisture content. Energy and Buildings, 2019, 202, pp.109340. 10.1016/j.enbuild.2019.109340. hal-02538653

Non-Fickian diffusion in biosourced materials: prediction of the delay between relative humidity and moisture content

A. Challansonnex[a], J. Casalinho[a], P. Perré[a,b]

[a]LGPM, CentraleSupélec, Université Paris-Saclay, 8-10 rue Joliot-Curie, 91 190 Gif-sur-Yvette, France
[b]LGPM, CentraleSupélec, Centre Européen de Biotechnologie et de Bioéconomie (CEBB), 3 rue des Rouges Terres, 51 110 Pomacle, France

---

Abstract

This work focuses on non-Fickian diffusion in biosourced building materials. To study these memory effects in this kind of materials, an original and automatic device was conceived and built. It allows a series of samples to be submitted, simultaneously, to a perturbation of RH at its front face and to record the evolution of sample mass and of RH at its back face. When analyzed using a classical heat and mass transfer model, the experimental data depicts a delay between RH and moisture content, the RH evolution being too fast. To address this problem, a new formulation able to model those types of behaviors using memory functions was used. To test the predictive potential of the new formulation, these memory functions were not identified but taken from a previous work, where they were determined experimentally using minute samples. A full set of experiments performed with Low Density Fiberboard (LDF) and Medium Density Fiberboard (MDF) was simulated using this new formulation feed by the experimental memory functions. The good agreement found between simulated and experimental results proves the predictive potential of the new macroscopic formulation.

Keywords: building, coupled transfer, energy, experiment, fading memory, macroscopic formulation, renewable materials

---

1. Notations

The main notation are summarized in tables 1 to 3.

2. Introduction

In recent decades, there has been a strong interest in bio-based materials in the construction industry. They can be found in many forms and used in many applications, including solid wood for the structure, fibrous materials (wood fibres, straw, etc.) for insulation or hemp concrete for mixed use. This interest is partly due to the low carbon footprint of these materials of plant origin (hence with carbon capture) and their renewable nature [1, 2, 3, 4]. But it is also due to their hygrothermal properties. Indeed, it has been shown that, thanks to their high hygroscopicity, these materials can help to regulate ambient humidity and thus improve indoor air quality or even reduce energy consumption [5, 6, 7]. However, when it comes to simulating their dynamic behaviour at the building or even laboratory level, significant differences are observed with the experiments [8, 9, 10]. These differences can have different origins, one of them being the parameters that feed the building energy simulations [11, 12]. For instance methodological errors in the vapor diffusivity measurement [13] or the non consideration of the hysteresis of the sorption isotherm [14, 15] are part of the issues currently explored. For fibrous insulation materials, significant errors in the kinetics of water vapour transfer within the materials can be explained by the absence of local thermodynamic equilibrium [16, 17, 18, 19]. Indeed, these materials consist of two phases with contrasting characteristics. The gaseous phase which is highly diffusive and well connected and the solid phase (the fibers) which is poorly diffusive. The microscopic diffusive time inside the fibers can therefore be of the same order of magnitude than the macroscopic diffusive time, which explains the possibility of non-local equilibrium. The consequences of this phenomenon are manifold. One can cite the dependency with thickness of the macroscopic vapor diffusion coefficient in transient state [20], the different values obtained when measured in transient or steady state [21] or non-physical

Table 1: List symbols (Latin letters)

Symbol	**Name**	**Unit**
a_w	sorption isotherm (water activity)	-
c	molar concentration	$mol.m^{-1}$
$\boldsymbol{D}$	diffusion tensor	$m^2.s^{-1}$
$\boldsymbol{f}$	dimensionless diffusion factor	-
h	specific enthalpy	$J.kg^{-1}$
h	heat transfer coefficient	$W.m^{-2}.K^{-1}$
$\boldsymbol{J}_k$	diffusive flux of component k	$kg.m^{-2}.s^{-1}$
$\boldsymbol{J}_q$	heat flux	$W.m^{-2}$
K	intrinsic permeability	m^2
k	relative permeability	-
k	mass transfer coefficient	$m.s^{-1}$
L_v	specific enthalpy of evaporation	$J.kg^{-1}$
M	molar mass	$kg.mol^{-1}$
$\boldsymbol{n}$	normal unit vector	-
p or P	pressure	Pa
q_k	diffusive flux of component k	$kg.m^{-2}.s^{-1}$
q_h	heat flux	$W.m^{-2}$
R	gas constant	$J.mol^{-1}.K^{-1}$
S_k	objective function for variable k	-
T	temperature	$^{\circ}C$
$\boldsymbol{v}$	general velocity vector	$m.s^{-1}$
X	solid moisture content (dry basis)	-

Table 2: List of symbols (Greek letters)

Symbol	**Name**	**Unit**
α	proportion terms of memory function	-
ε	volume fraction	-
φ	memory function	-
λ	thermal conductivity	$W.m^{-1}.K^{-1}$
μ	vapour resistance ratio	-
ρ	density	$kg.m^{-3}$
∂	partial derivative	-
∇	gradient	-
$\nabla\cdot$	divergence	-
ω	mass fraction	-
ψ	gravitational potential	s^{-2}
τ	time constants of memory function	s

Table 3: Subscripts and superscripts

Subscripts	**Meaning**
a	air
b	bound water
eff	effective property
eq	at equilibrium
exp	experimentally obtained
g	relative to the gaseous phase
$pred$	predicted by model
s	solid
v	water vapour
vs	saturated water vapour
w	liquide water
∞	at large distance from interface

Superscript	**Meaning**
$\overline{\psi}$	averaged of variable ψ over the REV
$\overline{\psi}^{\ell}$	intrinsic average of ψ over phase ℓ

values of the identified water vapour diffusivity [22]. The presence of a phase shift between relative humidity and moisture content, as reported in [23] is also likely to be explained by this phenomenon. Indeed, because of the delayed diffusion inside the fiber, RH is ahead of moisture content. Consequently, in building energy simulations, this phenomenon generates errors on the quantity of vapour transferred and on the moisture quantity stored inside the walls. In turn, due to the latent heat of evaporation, this induces important errors in the energy demand.

The first objective of this work was to establish a reliable experimental dataset to unquestionably confirm the existence of memory effects at the scale of centimetric samples. Our strategy is to prove that a simple macroscopic model is not able to fit the experiment, which requires at least two independent physical parameters to be measured simultaneously. To achieve this goal, an original and automatic device was conceived and built. It allows a series of samples to be tested simultaneously. Each sample is submitted to a perturbation of RH at its front face and the evolution of sample mass and of RH at its back face are continuously recorded.

The data collected by this new device confirms the memory effects : a classical heat and mass transfer model is not able to predict correctly, at the same time, the evolution of averaged moisture content and the RH at back-face.

To overcome this problem, a new macroscopic formulation able to consider the memory effects using kernel functions was used [24]. This formulation is embedded in a comprehensive model considering the coupling between heat and mass transfer (H&M). The comprehensive formulation is solved by the in-house computational code *TransPore* [25, 26]. In a previous study [27], very thin samples of biosourced materials were submitted to variations in ambient RH while their mass were recorded. The memory functions that represent the microscopic diffusive behavior of the materials were defined from these experiments by inverse analysis.

In the present work, these memory functions were used as input data in the new macroscopic model. Finally, just one parameter was identified using the

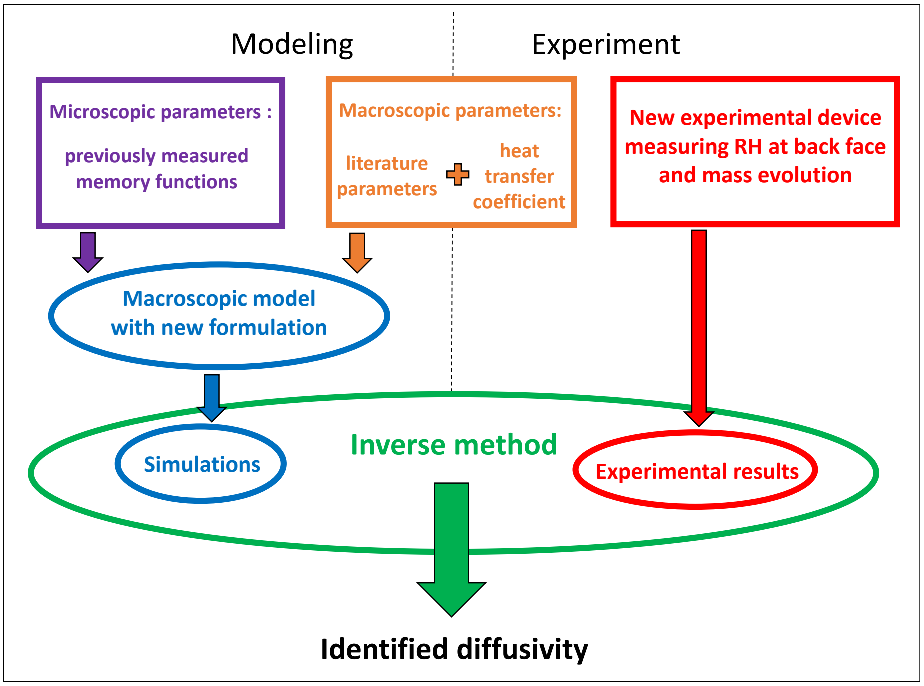

Figure 1: Principle of the identification procedure

new dataset : the macroscopic water vapour diffusivity. All other macroscopic values (intrinsic permeability, sorption isotherms, thermal conductivity...) come from previously published works and the external heat transfer coefficient was determined experimentally. A full set of experiments performed with LFD (Low Density Fiberboard) and MDF (Medium Density Fiberboard) was simulated using this new formulation feed by the experimental memory functions. A good agreement was found between simulated and experimental results. This strategy, developed to prove the predictive potential of the new formulation, is summarized in Fig 1.

3. Materials and methods

3.1. Materials

The materials that were studied in this work are low density fiberboard (LDF) and medium density fiberboard (MDF). LDF is a fibrous material used for insulation. It is made of wood fibres agglomerated by their bonding properties during the so-called wet process [28]. Its hygrothermal properties have been widely studied [29, 30, 31, 32, 33]. In this work, panels of LDF with different thickness and densities are studied, all produced by Steico (Munich, Germany). Testing different thickness is important in the context of this research as the effect of non local equilibrium should be greater with thin panels. Indeed, the macroscopic characteristic time increases as the thickness squared and eventually becomes higher than the microscopic characteristic time. Therefore, the material becomes progressively homogenisable.

The three different panels characteristics are as follow, all densities being measured at 40% RH:

- a $20mm$ thick panel with a density of $145kg.m^{-3}$,
- a $10mm$ thick panel with a density of $255kg.m^{-3}$,
- a $20mm$ thick panel with a density of $222kg.m^{-3}$.

Note that although the two last panels have different densities, they are sold under the same commercial name.

Contrary to LDF, MDF is made of wood fibres tied by an adhesive : fibres, urea-formaldehyde resin and paraffin wax are processed at high temperature and pressure to manufacture panels [34]. This produces a structural material mostly used for internal decoration and furniture. Its hygrothermal properties were also widely studied [35, 36]. In this work, a $10mm$-thick panel with a density of $655kg.m^{-3}$ was studied.

Disk-shaped samples with a diameter of $72mm$ were cut from those panels. As in previous studies [37], the samples were coated with an aluminum foil glued to the lateral faces by epoxy resin to avoid lateral water vapor leakage. A photograph of the different types of samples is depicted in Fig. 2.

3.2. Experimental setup

The principle of the measurement is to impose a sudden perturbation of RH at the front face of the sample which will create a transient diffusive flux through

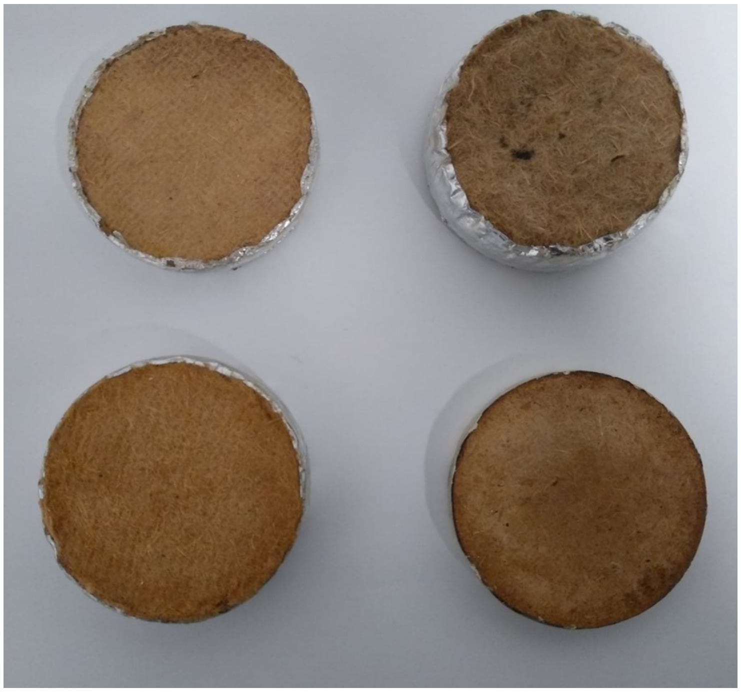

Figure 2: Photograph of the samples: From left to right and top to bottom: LDF-255kgm^{-3}-10mm, LDF-145kgm^{-3}-20mm, LDF-222kgm^{-3}-20mm, MDF-655kgm^{-3}-10mm

it. During the test, the sample mass and the RH at its back face are measured and recorded. As sorption tests are time consuming, we designed an original experimental setup able to measure these two pieces of information simultaneously on several samples. Fig 3 depicts a CAD 3D model of the setup (a) and a general view of its realisation (b). The automatic device was conceived to measure sequentially the mass and the RH at back-face of each sample without any wires that would perturbate weighing. To do so, the sample is placed in a support which includes a RH/temperature sensor positioned at its back face. This sensor is connected to a target at the top of the support. Thus, it is possible to acquire the evolution of RH at the back face of the sample by ensuring a temporary contact between this target and electrical contactors during an upward motion (Fig 4a). For the weighing stage, the support is placed on the weighing plate during a downward motion (Fig 4b). The design includes a crown-shaped holder. Along the test, the crown rotates to measure successively each sample. Up to eight samples can be placed simultaneously which is very useful considering that the necessary observation time can be as long as some weeks. The following subsections give additional details on the experimental device and test protocol.

3.3. Climatic Chamber

This in-house climatic chamber, built from an insulated container (Froid Loisir Equipement, Saillans, France), is divided in two volumes by a vertical plate: an operational chamber that contains the setup and a narrow rear chamber for temperature and relative humidity control. The temperature control is ensured by a regulated heating resistance and the relative humidity is ensured by an air flow forced against a water film set at the dew point temperature. The water is pumped from a thermocryostat (Ministat230, HUBER, Offenburg, Germany) to the top of the rear chamber where it flows along a plate. Three ventilators ensures the air flow. Two RH/temperature sensors (Sensirion SHT75, HDI Electronics, Pérois, France) are placed at opposite corners of the climatic chamber in order to record its average conditions. In Fig 5, one can see the evolution of the average RH and temperature inside the climatic chamber while performing a stepwise change in RH from 40 to 60 %. It takes ca. 10 minutes for the thermocryostat to reach the targeted temperature. At this time, the change in RH already reached 90 % of its total change. The targeted value is obtained after ca. one hour, when the temperature has decreased to its equilibrium value. One can observe that, once the conditions are constant, the regulation allows very stable conditions to be obtained, both in RH and temperature.

3.4. Sample supports

The sample support was designed and manufactured to fulfill several functions : i) to allow the sample to be weighted without perturbation, ii) to insure a temporary contact for RH measurement and iii) to insure a good exposure of the sample front-face to the chamber conditions (Fig 6). The holder and impervious-disk designs are based on previous studies ([22], [37]). The impervious-disk which has the same diameter as the sample has a small cavity which contains a SHT75 temperature/humidity sensor. This disk is inserted against the sample inside the holder whose internal diameter is larger. To ensure air tightness, a rubber tube whose internal diameter is smaller than the sample has been previously fixed inside the holder. A small hole in the holder lateral face allows a vacuum pump to be plugged between the rubber tube and the holder internal face. The under-pressure presses the rubber against the holder face, so that the sample/disk assembling can be inserted. When the vacuum pump is unplugged, the rubber tube squeezes the lateral face of the sample/disk ensuring airtightness is spite of dimensional changes of the sample. The sensor is linked to the target at the top of the support which transmits the information during the temporary contact. It is important to mention that two precautions are required to ensure perfect air-tightness : two coats of resin epoxy are applied on the lateral face of the sample before the test and some void grease is put between the rubber tube and the epoxy surface when placing the sample into the support. This airtightness was checked using an impervious sample (a PVC sample) as tested material . In this case, the change of RH value at back face following a sudden change of RH in the climatic chamber is hardly detectable (typically 0.1 % of RH change over 5 hours).

The support is perfectly centered inside the crown sample holder thanks to a conical shape. This ensures two functions :

- to avoid any friction when the crown gets downwards for weighing (Fig 4b),
- to ensure an accurate contact between the target and the contactors when the crown moves upwards for RH measurement (Fig 4a).

3.5. General assembly

The general assembly can be observed in Fig 3a. The crown holding all samples can move vertically to ensure weighing and RH measurement and can rotate to deal successively with each sample. This is ensured respectively by an electromechanical actuator (EMC32-12, Rexroth, Lohr am Main, Germany) driven by a DC motor and a precision rotation stage (M-URM80, Newport Corporation, Irvine, United States). Three vertical positions are secured: i) the upper position for temporary contact with the RH sensor, (Fig 4a), ii) the lower position to put the sample on the weighing plate (Fig 4b) and the intermediate position allowing a free rotation of the crown.

To preserve the electronic balance from the chamber conditions, the balance (EP6102C, Ohaus, Greifensee, Switzerland, precision of $0.01g$) is placed beneath the climatic chamber. A stable and adjustable support secured on the balance plate holds a glass rod crossing the chamber wall without friction. The internal weighing plate is then fixed on this rod. A glass rod presents a good stiffness together with a low thermal conductivity, required to avoid condensation nearby the chamber wall.

3.6. Experimental Protocol

The whole setup is remotely controlled using a software developed in *Microsoft Visual Basic*. For each sample, a first acquisition of RH at the back

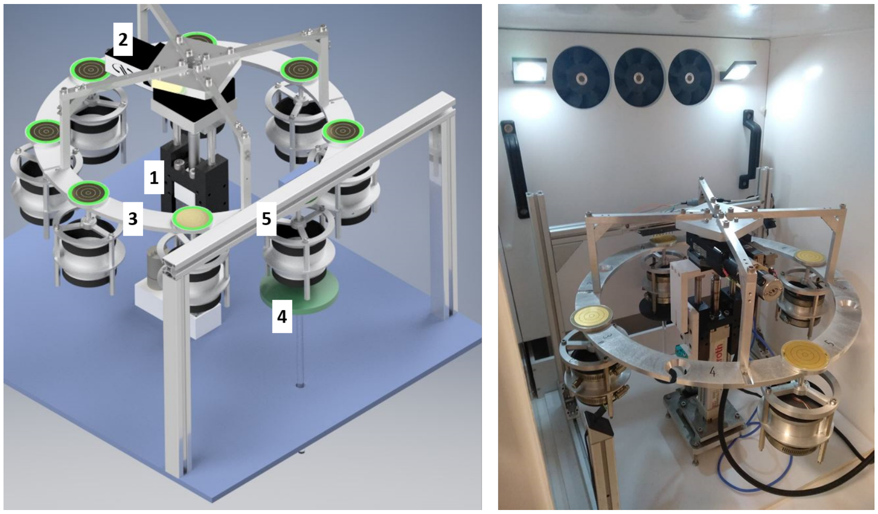

Figure 3: Left:a) CAD representation of the setup with: 1)Electromechanical cylinder, 2)Horizontal motor, 3)Crown, 4)Weighing system, 5)Structure for RH acquisition, Right:b) Photograph of the whole setup in the climatic chamber

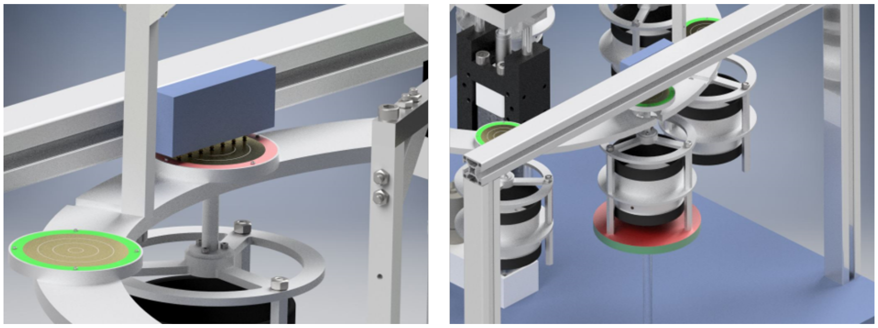

Figure 4: Left a): Sample support in upper position, the contact between the target (in red) and the contactors allows the acquisition of RH at the back face of the sample, Right b): Sample support in lower position, the sample support is placed on the weighing plate (in red).

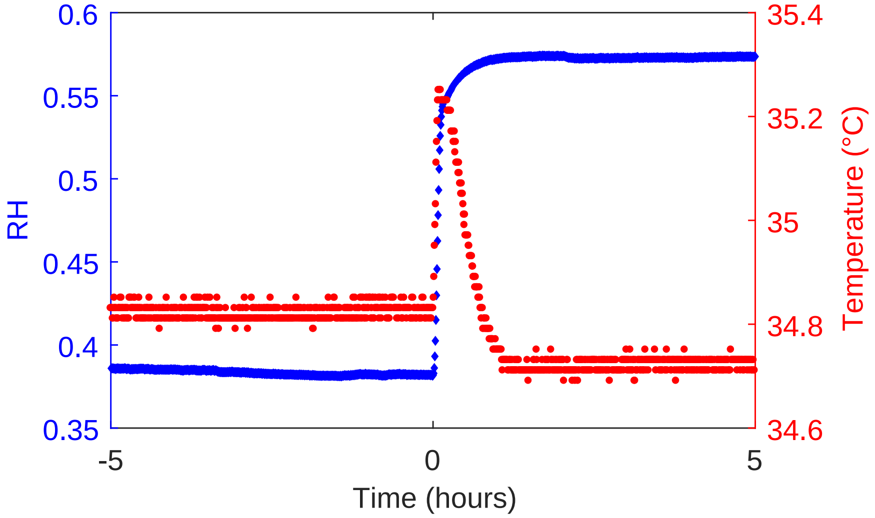

Figure 5: Evolution of RH and temperature inside the climatic chamber during a RH step from 40 to 60 %

face of the sample is done by placing the target against the contactors. The ventilation is then shut down to lower the weighing noise. After taring, the support is placed on the weighing plate. After mass acquisition, the ventilation is switched on and another RH acquisition is perfomed. The support is then placed in intermediate position to allow rotation to proceed to the next sample. The RH value used as raw data is the average of the measurements before and after weighing and is allocated to the weighing time. Once all samples have been treated, the rotation stage comes back to its reference position. The device is ready for another data collection.

In this work two samples of each kind were tested (referred as sample A and B). Thus, a total of eight samples were tested during two different experiments (four samples per experiment). In the first experiment, materials with a lower macroscopic diffusive time were tested: LDF $20mm$ thick with a density of $145kg.m^{-3}$ and LDF $10mm$ thick with a density of $255kg.m^{-3}$. In the second experiment $20mm$ thick LDF with a density of $222kg.m^{-3}$ and MDF were tested. In order to avoid hysteresis effects and yet ensure the reproducibility of the

Figure 6: Left a) Exploded view of the 3D model with: 1) Target, 2) Cone, 3) Rod, 4) Upper part, 5) Holder (with rubber tube inside), 6) Spacer, 7) Impervious disk, 8) Sample, Right b) Photograph of the sample support.

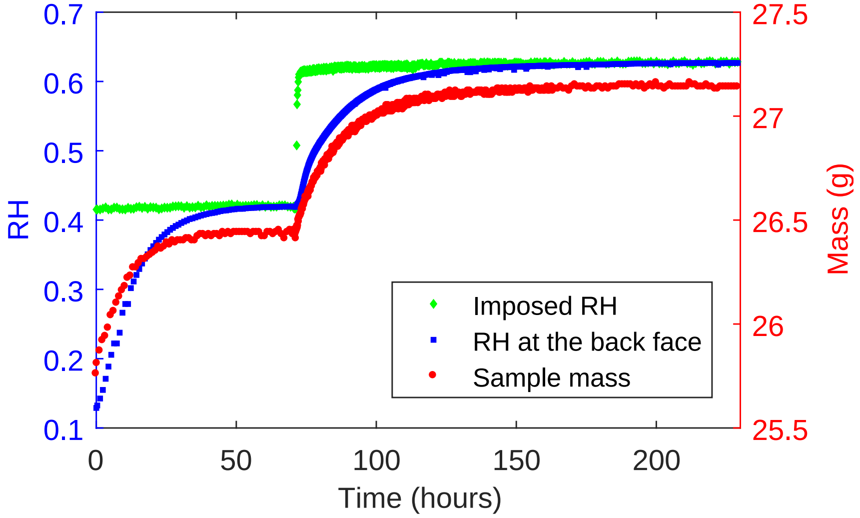

Figure 7: Example of raw data obtained for MDF: actual RH value in the climatic chamber, RH at the back face and sample mass.

experiment, samples were first dried in a desiccator at room temperature to a RH close to zero using a nitrogen flow. The samples were then placed in their support inside the experimental device and the acquisition was launched. The presented experiment consists of two isothermal periods (35°C):

- A plateau at 40 % RH until stabilization of the mass and RH on the back faces,
- A plateau at 60 % RH after a sudden increase in the RH to this new value until stabilization of the mass and RH on the back faces.

The acquisition rate is adapted during the test, from a rapid rate after the sudden change in the RH of the chamber to slower rates as the samples approach equilibrium. Typically, during the first stabilization plateau, the rate is one acquisition per hour. This rate increases at one acquisition every 8 minutes for the first 24 hours after sudden change in RH, every 16 minutes until 72 hours and then every 1 hour again. Examples of raw data are plotted in Fig 7.

3.7. Determination of the external heat transfer coefficient

The heat and mass transfer coefficients between the sample surface and the climatic chamber play a role in the global resistance to transfer [26]. Consequently, its effect may interfere with the internal resistances in the identification procedure. In order to be consistent with our predictive strategy, we decided to experimentally determine the resistance to transfer at the interface rather than an indirect determination by inverse analysis. Assuming the analogy between heat and mass transfer in the boundary layer [38], the heat transfer coefficient can be deduced from the drying rate during the constant drying rate (CDR) period provided this period is long enough to assume a steady temperature field. Obviously, as the transfer coefficients depend on the configuration (velocity and geometry), the experimental configuration must be exactly the same as in the actual experiments. To ensure this constraint while obtaining a long CDR period, a PVC disk was covered on its front face with a sponge saturated with water and placed in a sample support. During a well-established CDR period, the product is at constant temperature and the heat flux is just used for water evaporation. Assuming the heat transfer coefficient h to be the same on both sides of the sample, the energy balance during a steady CDR period reads as:

$$L_v Q_v = S(h + (h^{-1} + \ell/\lambda)^{-1})(T_d - T_w) \tag{1}$$

Where L_v is the latent heat of vaporization of water, Q_v the drying rate determined by weighing, S the surface area of the sample, λ the thermal conductivity of PVC, ℓ the thickness of the PVC disk, T_w the wet bulb temperature and T_d the dry bulb temperature. Using equation (1) during a well established CDR period allowed the value of h to be determined ($h = 8.9 W.K^{-1}$). This value will be used in what follows as input parameter. Consistently, the same value, together with the thermal resistance of the PVC disk, is used on the back-face of the sample. This is important to consider correctly the heat and mass transfer coupling inside the sample [39].

4. Theoretical model

4.1. Memory functions

Memory effects occurring in biosourced materials are explained by two additional effects : possible dual-cale phenomena arising when the conductive phase is not the storage phase and molecular relaxation arising at the macromolecular level. In a theoretical paper [24], we proved that both effects could be transferred as additive effects at the macroscopic scale. Based on this result, the cumulative memory function was characterized from experiments performed on minute samples [27]. The global memory function $\varphi(t)$ is defined as the evolution of the moisture content (water in the storage phase) after a sudden change from RH_{ini} to RH_{fin}. Considering that, in practical situations, RH varies continuously rather than stepwise, the variation of moisture content should be expressed through a convolution product:

$$X(t) - X_{ini} = \int_0^t \varphi(t-\tau)\frac{\partial X_{eq}}{\partial \tau} d\tau \tag{2}$$

where X is the moisture content and X_{eq} is the equilibrium moisture content, defined by water activity. In equation 2,

$$\frac{\partial X_{eq}}{\partial \tau} d\tau = dX_{eq} \tag{3}$$

represents the variation of equilibrium moisture content during the infinitesimal time interval $d\tau$.

In order to ease the computational solution, the function $\varphi(t)$ was defined with the following expression:

$$\varphi(t) = 1 - \alpha_1 exp(-\frac{t}{\tau_1}) - \alpha_2 exp(-\frac{t}{\tau_2}) \tag{4}$$

where τ_1 and τ_2 are the time constants and α_1 and α_2 the respective proportions. The use of exponential function allows the convolution product to be treated by internal variables defined by simple ODEs [24]. Since LDF and MDF do not have the same composition, the values are different. For both materials,

Materials	α_1	τ_1 (s)	α_2	τ_2 (s)
LDF	0.38	3.2×10^3	0.13	2.6×10^4
MDF	0.45	2.3×10^3	0.02	4.1×10^4

Table 4: Values of the coefficients defining the memory function for both materials (identified in [27])

the parameter values of the memory function, as determined for a RH jump from 40 to 60 % in [27], are summarized in Table 4. These values were used as input data in all simulations of the present work.

4.2. Macroscopic formulation

The macroscopic formulation that was used in this work is based on a classical set of equations taking into account coupled heat and mass in porous media. More details about it can be found in [25, 26]. Those equations were modified to consider the absence of thermodynamic equilibrium [24]. In the new formulation, equation (2) is used to express the derivative of moisture content with respect to time. Thus, the set of macroscopic equations becomes :

Moisture conservation

$$\rho_s \frac{\partial}{\partial t}\left(\int_0^t \varphi(t-\tau)\frac{\partial X_{eq}}{\partial \tau} d\tau\right) + \nabla \cdot (\rho_v \bar{\boldsymbol{v}}_g) = \nabla \cdot (\rho_g \boldsymbol{f} \boldsymbol{D}_v \cdot \nabla \omega_v) \tag{5}$$

Energy conservation

$$\begin{aligned}\frac{\partial}{\partial t}\left(\varepsilon_g(\rho_v h_v + \rho_a h_a) + \overline{\rho}_b \overline{h}_b + \varepsilon_s \rho_s h_s\right) \\ + \nabla \cdot ((\rho_v h_v + \rho_a h_a)\bar{\boldsymbol{v}}_g) \\ = \nabla \cdot (\lambda_{eff} \nabla T + \rho_g \boldsymbol{f} \boldsymbol{D}_v (h_v \nabla \omega_v + h_a \nabla \omega_a))\end{aligned} \tag{6}$$

Air conservation

$$\frac{\partial \left(\varepsilon_g \rho_a\right)}{\partial t} + \nabla \cdot (\rho_a \bar{\boldsymbol{v}}_g) = \nabla \cdot (\rho_g \boldsymbol{f} \boldsymbol{D}_v \nabla \omega_a) \tag{7}$$

Transport equations

$$\bar{\boldsymbol{v}}_g = -\frac{\boldsymbol{K}\boldsymbol{k}_g}{\mu_g}(\nabla p_g - \rho_g \nabla \psi_{\boldsymbol{g}}) \tag{8}$$

Boundary conditions

$$\begin{aligned} &\boldsymbol{J}_w\big|_{x=0^+} \cdot \boldsymbol{n} = k\, c\, M_v \, \ln\left(\frac{1 - x_\infty}{1 - x_v\big|_{x=0}}\right) \\ &\boldsymbol{J}_q\big|_{x=0^+} \cdot \boldsymbol{n} = h\left(T\big|_{x=0} - T_\infty\right) \\ &P_g\big|_{x=0^+} = P_{atm} \end{aligned} \tag{9}$$

One should note that the value of the partial pressure of water vapour is related to the equilibrium moisture content X_{eq} through the sorption isotherm (or water activity) $p_v = p_{vs}(T) \times a_w(T, X_{eq})$.

The comprehensive set of equation proposed in [24] was adapted to the configuration of interest, hence simplified, thanks to the following assumptions:

- since the samples remain in the hygroscopic domain, all liquid water contributions have been discarded,
- due to the particular morphology of the studied materials, a very large majority of the transfer occurs in the gaseous phase. Consequently, the transport terms of bound water have also been discarded,
- the effective diffusivity is expressed as a proportion of the binary diffusivity of vapour in air : $\boldsymbol{D}_{eff} = \boldsymbol{f}\boldsymbol{D}_v$, where $\boldsymbol{f}$ is a dimensionless diffusivity tensor. Note that along one given direction, $f = 1/\mu$ where μ is the *vapour resistance ratio* used for building materials.

Using a suitable computational strategy, this set of equations is able to simulate the coupling between heat and mass occurring during transfer in building materials while taking into account the absence of thermodynamic equilibrium. It allows three independent variables to be computed in space and in time (for example, temperature or enthalpy, moisture content, air density or gaseous pressure).

4.3. Inverse analysis

The principle of the inverse procedure is to feed the computational code with known parameters and to determine the unknown parameters by minimising an objective function. As our intend is to prove the prediction potential of the new formulation, only two parameters were identified : the initial moisture content X_{ini} identified only to reduce the residue and the dimensionless diffusivity f, whose identification results in a characterisation of the material. The sample characteristics (thickness, density, porosity) were simply measured and supplied to the computation code. The sorption isotherm and the effective permeability come from recent papers [33, 40]. The thermal conductivity is determined by a mixture law using the gaseous and solid volume fractions and their conductivities [41]. The relevance of the value given by this law was confirmed in [39]. Using the actual chamber conditions (temperature and RH) recorded during the test and the external heat transfer coefficients as determined in section 3.7, the physical model computes all variable fields versus time. It is therefore able to give the mean water content of the sample X and the RH at its back face. This allows two objective functions S_X and S_{RH} to be derived to quantify the difference between experimental and predicted values using the mean square distance as norm:

$$S_X = \sqrt{\frac{\sum_{i=1}^{N}[X^*_{exp}(t_i) - X^*_{pred}(t_i)]^2}{N}} \tag{10}$$

$$S_{RH} = \sqrt{\frac{\sum_{i=1}^{N}[RH_{exp}(t_i) - RH_{pred}(t_i)]^2}{N}} \tag{11}$$

where X^*_{exp} is the dimensionless moisture content from the experiment, X^*_{pred} is the dimensionless moisture content predicted with estimated parameters, RH_{exp} is the experimental value of RH, RH_{pred} is predicted value of RH, t_i is the time of the ith acquisition and N the number of instants used in the minimization. The dimensionless value of moisture content was used to correct the small differences that may appear between the sorption isotherm supplied to the code and the equilibrium moisture content obtained for each individual sample. Accurately defined here thanks to the long duration of our experiments, it varies from 0 for the equilibrium moisture content at RH_{ini} to 1 for the equilibrium moisture content at RH_{fin}.

The global objective function S is a linear combination of those two functions:

$$S = \beta \times S_X + (1 - \beta) \times S_{RH} \tag{12}$$

A value of $\beta = 0.2$ was used as best compromise between the two variables. It corrects for the difference in variation range of the two variables (0.2 for RH and 1 for the dimensionless MC). A Nedler-Mead algorithm was used to minimise this objective function and find the best set of parameters (X_{ini} and f). Here, the identification starts five hours before the RH jump. At this moment the moisture content is already stabilized at its equilibrium value. The identification ends 50 hours after the perturbation for the two more diffusive samples, 130 hours after for the less diffusive samples. In both cases, the samples were almost at equilibrium.

5. Results and discussion

Without memory effects, the simulation uses a classical, yet comprehensive, set of coupled heat and mass transfer. In the case of LDF at $145 kg.m^{-3}$, the most diffusive material, the RH information travels very fast from the climatic chamber to the sample core, faster than diffusion inside fibres. Dual-scale effects are obvious and it is not possible to fit the two pieces of information (RH_{back} and X) simultaneously. The identification procedure simply tries to decrease the global objective function by a compromise between the two variables. As a result, the RH evolution is too slow and the moisture content too fast (green curves in Fig. 8). With an average value of 0.332, the dimensionless factor identified without memory effects is lower than the published values for this material, either measured in steady-state experiments [20, 32] or predicted by upscaling from the real pore morphology [41].

On the contrary, when using the new formulation with memory effect, the model is in very good agreement with the experimental data for both RH and moisture content (blue curves in Fig. 8). Thanks to the memory effects, the identified diffusivity (average value of 0.573) is now consistent with literature data, even though the experiment is performed in transient state. Keeping in mind that the memory functions were not identified but measured on minute samples, these good results (simultaneous prediction of two variables and consistent value of f) confirm that the new formulation perfectly accounts for all important physical phenomena. In particular, this includes the coupling between heat and mass transfer and the fading memory resulting from dual-scale effects and molecular relaxation.

For each sample, the identification of the effective diffusivity was performed without and with memory effects. The identified dimensionless diffusivities f as well as the residues between the model and the experiment for RH (S_{RH}) and dimensionless moisture content (S_X) are summarised in Table 5. In order to focus on the transient period during which the formulation matters, the residues were calculated over the first hours after the RH step (20 hours for the two most diffusive materials and 35 hours for the others). In general, the residues are dramatically reduced when using the memory function with an average decrease by a factor 7 for S_{RH} and 1.5 for S_X. The lower factor obtained for S_X is partly explained by the noise of the experimental mass. Anyway, as the additional information embedded in the new formulation is not an additional degree of freedom, these good results confirm the previous comment regarding the 20-mm thick LDF sample. It demonstrates that the observed phase shift originates from the microscopic diffusive behaviour and validates the new formulation. For each material, one might notice, sometimes, a significant scattering of the identified values of f between samples A and B. This is not surprising, as important scattering of vapour diffusivity has already been reported in literature for those types of biosourced materials [32]. Thus, the determination of an average macroscopic parameter suitable for building energy simulation would require more repetitions, which the experimental device makes it possible to do

Material	Sample	Formulation	f	S_{RH}	S_X
LDF 20 mm $145\ \mathrm{kg \cdot m^{-3}}$	A	Classic	0.366	1.62×10^{-2}	2.90×10^{-2}
		With memory	0.667	2.11×10^{-3}	2.09×10^{-2}
	B	Classic	0.298	1.92×10^{-2}	3.65×10^{-2}
		With memory	0.480	3.17×10^{-3}	2.32×10^{-2}
LDF 10 mm $255\ \mathrm{kg \cdot m^{-3}}$	A	Classic	0.171	1.94×10^{-2}	3.55×10^{-2}
		With memory	0.306	2.94×10^{-3}	2.68×10^{-2}
	B	Classic	0.169	2.25×10^{-2}	4.08×10^{-2}
		With memory	0.302	6.00×10^{-3}	2.70×10^{-2}
LDF 19 mm $234\ \mathrm{kg \cdot m^{-3}}$	A	Classic	0.347	1.34×10^{-2}	2.55×10^{-2}
		With memory	0.478	2.95×10^{-3}	2.15×10^{-2}
	B	Classic	0.267	1.93×10^{-2}	4.29×10^{-2}
		With memory	0.341	8.41×10^{-3}	3.32×10^{-2}
MDF 10 mm $655\ \mathrm{kg \cdot m^{-3}}$	A	Classic	0.0482	1.81×10^{-2}	3.55×10^{-2}
		With memory	0.0497	1.79×10^{-2}	2.50×10^{-2}
	B	Classic	0.0752	2.23×10^{-2}	3.12×10^{-2}
		With memory	0.0785	1.82×10^{-2}	2.80×10^{-2}

Table 5: Identified diffusivity and residues with or without memory functions

in a simple way. One has however to mention that this scattering is due to the variability of the material morphology at the spatial scale of laboratory characterisation : neglecting the heat and mass coupling or the dual scale effects would add an important systematic error to this variability. Such a biais would never be corrected, whatever the number of tested samples.

The results obtained for the 10-mm thick LDF samples with a density of $255kg.m^{-3}$ depict the same trend (Fig. 9). Once again, the classic formulation is not able to fit both quantities whereas the fit is excellent when using the memory function. In spite of the change in density and morphology, the same memory function works perfectly. This is consistent as, whatever its density, the LDF has the same microscopic composition. This also proves that the memory functions

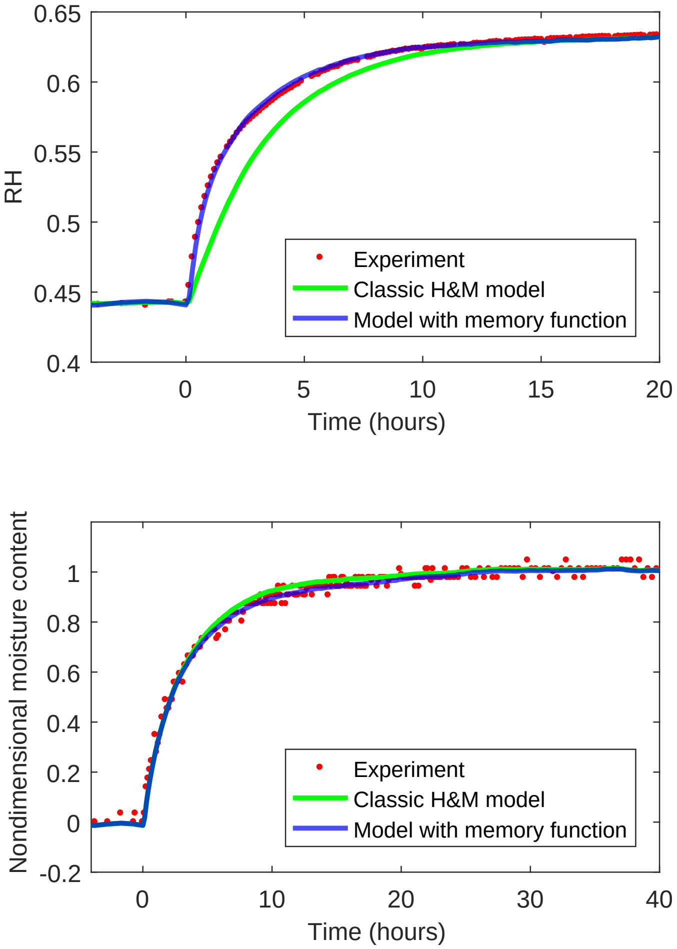

Figure 8: Comparison between simulation and experiment for sample A of LDF-20mm-$145 kg.m^{-3}$: (a) RH evolution at the back face (top), (b) dimensionless average moisture content (bottom).

are representative of microscopic effects, that just need to be characterised once. Besides, the morphology influences the macroscopic behaviour: with an average value of 0.304, the identified diffusivities are lower for this material than the previous one. Again, it is in good agreement with what was measured for similar materials [20]. The residues reduction when accounting for memory effects is similar to the previous material (a factor 5 for S_{RH} and 1.4 for S_X).

The 20-mm thick LDF sample with a density of $222kg.m^{-3}$ suggests similar comments (Fig 10). Again, the agreement is excellent with memory effects. The average value of the identified diffusivity (0.404) lies between the two previous ones which is consistent with the material densities. However, one can note that even though the residues are still lower when using memory function, the difference between the two simulations is less important than for 10-mm thick samples (reducing factors of 3.6 for S_{RH} and 1.4 for S_X). The memory effect is then less important in this case. Since this macroscopic diffusive time increases as the thickness squared and with the smaller f value compared with $145kg.m^{-3}$ LDF samples, more time is allowed to the fibre to approach equilibrium. The dual-scale mechanisms progressively vanished at increasing thickness. A further increase of the thickness would have also reduced the effect of molecular relaxation (the longest time constant of Table 4). In spite of this fact, the use of memory functions still considerably ameliorates the results at short times. This is of great interest for building materials submitted to day and night alternation.

In the case of MDF, the simulation results with or without memory effects are similar (Fig 11). When using the memory functions, the average residues only decrease by 9% for S_{RH} and 20% for S_X. This is not surprising as the high density of MDF dramatically reduces the diffusion at the macroscopic level: the average f value (0.064) is one order of magnitude lower than those obtained for LDF. Thus, even with a thickness of 10 mm, the macroscopic characteristic time is long enough to ensure local equilibrium. However, one must note that the model does not fit the experimental RH values. Even with memory effects, the residues remain important compared to the previous materials. Based on our predictive approach, one can affirm that this discrepancy can not be explained

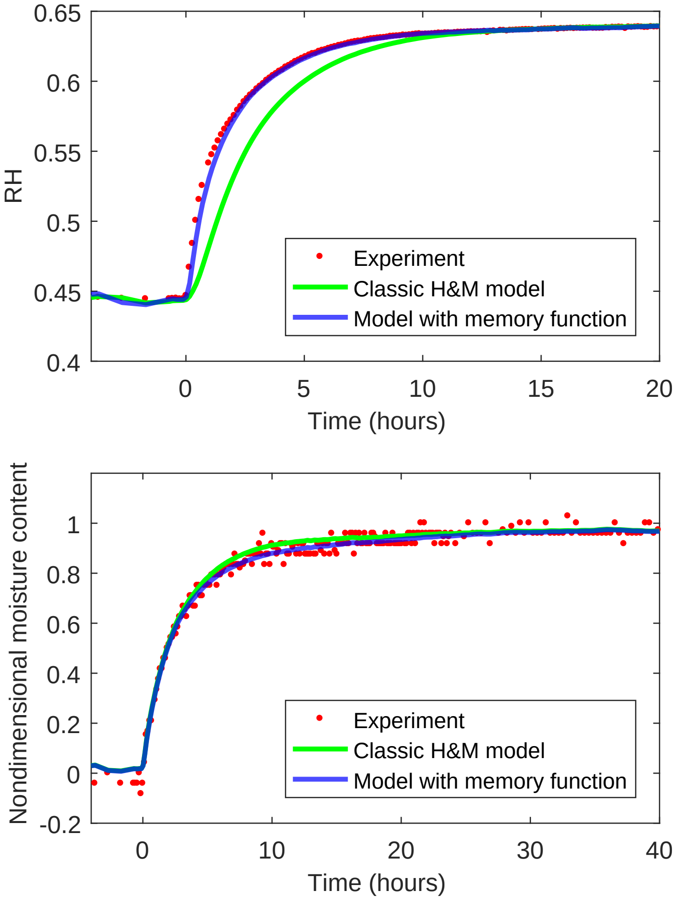

Figure 9: Comparison between simulation and experiment for sample A of LDF-10mm-$255 kg.m^{-3}$: (a) RH evolution at the back face (top), (b) dimensionless average moisture content (bottom).

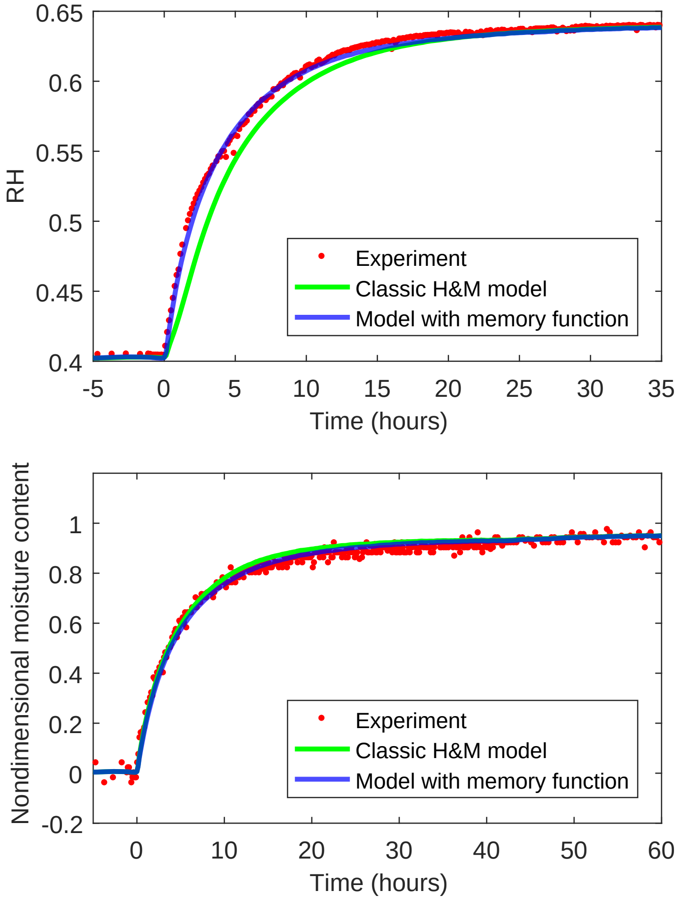

Figure 10: Comparison between simulation and experiment for sample A of LDF-20mm-$222 kg.m^{-3}$: (a) RH evolution at the back face (top), (b) dimensionless average moisture content (bottom).

by microscopic effects, as those effects are embedded in the memory function determined on minutes samples. Therefore, the origin of this difference has yet to be explained, formulated and predicted. As MDF is a structural material, we believe that the stress profile in the thickness could be the explanation: during adsorption, swelling occurs at surface while the sample core is still close to the initial MC with little dimensional change. Depending on the mechanical behaviour, the external part of the sample is therefore under compression and the sample core under tension. Besides, compressive stress or contrained deformations are known to decrease the equilibrium moisture content of wood or lignocellulosic products [42, 43, 44]. This coupling between local scale (stress field on sorption isotherm) and global scale (stress profile along the sample thickness) is likely to give rise to another effect able to produce a fading or permanent memory. Its time constant would be tied to the macroscopic parameters, including thickness, while its amplitude would be tied to both macroscopic and microscopic effects. This could explains the very long time constant observed in wood for example [45].

6. Conclusion and perspectives

This work is based on experimental results obtained with an original in-house device. This device was conceived to control the environment (temperature and relative humidity, RH) and to follow the evolution of several samples, by measuring simultaneously the RH on their back-face and their mass. Results are presented for LDF samples of different densities and thicknesses and for MDF samples. The experimental results were analysed by an inverse method using a comprehensive H&M model with non-Fickian effects. The following conclusions can be drawn :

- A classic H&M model is not able to predict correctly the evolution of both RH and moisture content for those materials, which denotes the presence of non-local equilibrium,

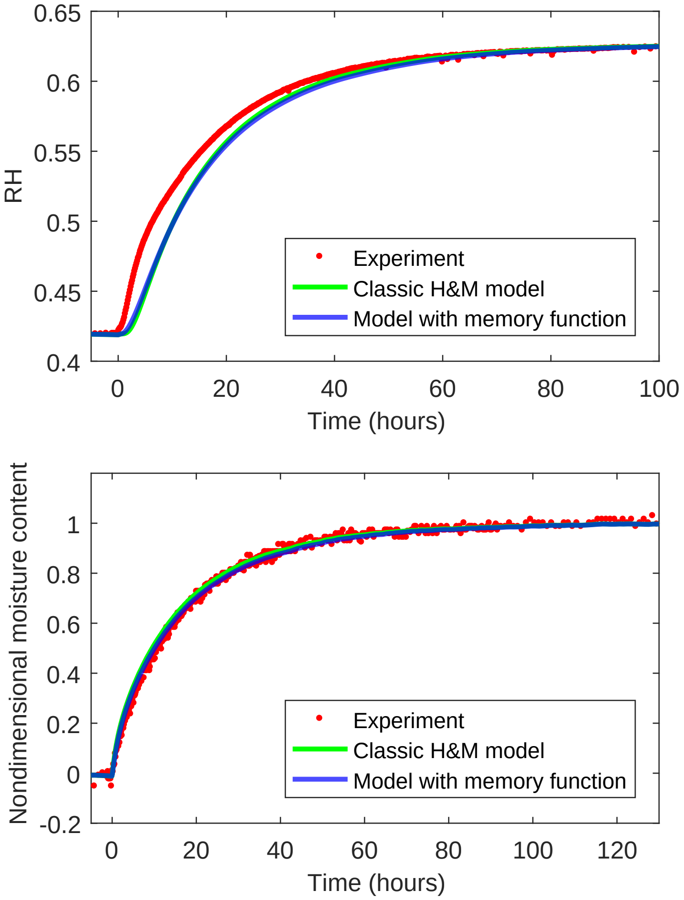

Figure 11: Comparison between simulation and experiment for sample A of MDF-10mm-655$kg.^{-3}$: (a) for RH evolution at the back face (top), (b) for dimensionless average moisture content (bottom).

- For LDF, the model using the new formulation remarkably predicts the evolution of both quantities when it is fed with memory functions determined on micro-samples,
- This novel and validated formulation allows the materials to be accurately characterised in transient state,

This work proves that the new formulation with non-Fickian effects is able to predict the diffusive behaviour of biosourced materials. This formulation should be used either at the lab scale for charaterisation or at the building scale to predict the energy demand.

References

[1] Y. Florentin, D. Pearlmutter, B. Givoni, E. Gal, A life-cycle energy and carbon analysis of hemp-lime bio-composite building materials, Energy and Buildings 156 (2017) 293–305. `doi:10.1016/j.enbuild.2017.09.097`.
URL `http://dx.doi.org/10.1016/j.enbuild.2017.09.097`

[2] P. Pawelzik, M. Carus, J. Hotchkiss, R. Narayan, S. Selke, M. Wellisch, M. Weiss, B. Wicke, M. K. Patel, Critical aspects in the life cycle assessment (LCA) of bio-based materials - Reviewing methodologies and deriving recommendations, Resources, Conservation and Recycling 73 (2013) 211–228. `doi:10.1016/j.resconrec.2013.02.006`.
URL `http://dx.doi.org/10.1016/j.resconrec.2013.02.006`

[3] D. Peñaloza, M. Erlandsson, A. Falk, Exploring the climate impact effects of increased use of bio-based materials in buildings, Construction and Building Materials 125 (2016) 219–226. `doi:10.1016/j.conbuildmat.2016.08.041`.

[4] A. D. La Rosa, A. Recca, A. Gagliano, J. Summerscales, A. Latteri, G. Cozzo, G. Cicala, Environmental impacts and thermal insulation performance of innovative composite solutions for building applications, Construction and Building Materials 55 (2014) 406–414. `doi:10.1016/j.`

`conbuildmat.2014.01.054`.
URL `http://dx.doi.org/10.1016/j.conbuildmat.2014.01.054`

[5] O. F. Osanyintola, C. J. Simonson, Moisture buffering capacity of hygroscopic building materials: Experimental facilities and energy impact, Energy and Buildings 38 (10) (2006) 1270–1282. `doi:10.1016/j.enbuild.2006.03.026`.
URL `http://www.sciencedirect.com/science/article/pii/S0378778806000855`

[6] M. Woloszyn, T. Kalamees, M. O. Abadie, M. Steeman, A. Sasic Kalagasidis, The effect of combining a relative-humidity-sensitive ventilation system with the moisture-buffering capacity of materials on indoor climate and energy efficiency of buildings, Building and Environment 44 (3) (2009) 515–524. `doi:10.1016/j.buildenv.2008.04.017`.

[7] J. A. Orosa, A. Baaliña, Improving PAQ and comfort conditions in Spanish office buildings with passive climate control, Building and Environment 44 (3) (2009) 502–508. `doi:10.1016/j.buildenv.2008.04.013`.
URL `http://www.sciencedirect.com/science/article/pii/S0360132308000759`

[8] J. Jacques, M. Labat, M. Woloszyn, Dynamic coupling between vapour and heat transfer in wall assemblies : Analysis of measurements achieved under real climate, Building and Environment 87 (2015) 129–141. `doi:10.1016/j.buildenv.2015.01.022`.

[9] T. Kalamees, J. Vinha, Hygrothermal calculations and laboratory tests on timber-framed wall structures, Building and Environment 38 (5) (2003) 689–697. `doi:10.1016/S0360-1323(02)00207-X`.

[10] H. Künzel, A. Holm, D. Zirkelbach, A. Karagiozis, Simulation of indoor temperature and humidity conditions including hygrothermal interactions with the building envelope, Solar Energy 78 (4) (2005) 554–561.

`doi:10.1016/j.solener.2004.03.002`.
URL `http://www.sciencedirect.com/science/article/pii/S0038092X04000507`

[11] L. Wang, H. Ge, Hygrothermal performance of cross-laminated timber wall assemblies: A stochastic approach, Building and Environment 97 (2016) 11–25. `doi:10.1016/j.buildenv.2015.11.034`.
URL `http://dx.doi.org/10.1016/j.buildenv.2015.11.034`

[12] C. Spitz, L. Mora, E. Wurtz, A. Jay, Practical application of uncertainty analysis and sensitivity analysis on an experimental house, Energy and Buildings 55 (2012) 459–470. `doi:10.1016/j.enbuild.2012.08.013`.
URL `http://dx.doi.org/10.1016/j.enbuild.2012.08.013`

[13] T. Duforestel, Des transferts couplés de masse et de chaleur à la conception bioclimatique: recherches sur l'efficacité énergétique des bâtiments, HDR, Université d'Artois (2015) 241.

[14] J. Kwiatkowski, M. Woloszyn, J.-J. Roux, Modelling of hysteresis influence on mass transfer in building materials, Building and Environment 44 (2009) 633–642. `doi:10.1016/j.buildenv.2008.05.006`.

[15] R. Rémond, G. Almeida, P. Perré, The gripped-box model: A simple and robust formulation of sorption hysteresis for lignocellulosic materials, Construction and Building Materials 170 (2018) 716–724. `doi:10.1016/j.conbuildmat.2018.02.116`.

[16] K. Krabbenhoft, L. Damkilde, Double porosity models for the description of water infiltration in wood, Wood Science and Technology 38 (2004) 641–659. `doi:10.1007/s00226-004-0253-5`.

[17] U. Nyman, P. J. Gustafsson, B. Johannesson, R. Hägglund, A numerical method for the evaluation of non-linear transient moisture flow in cellulosic materials, International Journal for Numerical Methods in Engineering 66 (2006) 1859–1883. `doi:10.1002/nme.1597`.

[18] P. Perré, Multiscale aspects of heat and mass transfer during drying, Transport in Porous Media 66 (1-2) (2007) 59–76. `doi:10.1007/s11242-006-9022-2`.

[19] P. Perre, Multiscale Modeling of Drying as a Powerful Extension of the Macroscopic Approach: Application to Solid Wood and Biomass Processing, Drying Technology 28 (8) (2010) 944–959. `doi:Doi10.1080/07373937.2010.497079`.

[20] R. Rémond, G. Almeida, Mass diffusivity of low-density fibreboard determined under steady- and unsteady-state conditions : Evidence of dual-scale mechanisms in the diffusion, Wood Material Science and Engineering 6:1-2 (2011) 23–33. `doi:10.1080/17480272.2010.515035`.

[21] A. Challansonnex, F. Pierre, J. Casalinho, P. Lv, P. Perré, Mass diffusivity determination of various building materials based on inverse analysis of relative humidity evolution at the back face of a sample, Submitted.

[22] P. Perré, F. Pierre, J. Casalinho, M. Ayouz, Determination of the Mass Diffusion Coefficient Based on the Relative Humidity Measured at the Back Face of the Sample during Unsteady Regimes, Drying Technology 33:9 (2015) 1068–1075. `doi:10.1080/07373937.2014.982253`.

[23] D. Lelievre, T. Colinart, P. Glouannec, Hygrothermal behavior of bio-based building materials including hysteresis effects: Experimental and numerical analyses, Energy and Buildings 84 (2014) 617–627. `doi:10.1016/j.enbuild.2014.09.013`.
URL `http://dx.doi.org/10.1016/j.enbuild.2014.09.013`

[24] P. Perré, Coupled heat and mass transfer in biosourced porous media without local equilibrium : a macroscopic formulation tailored to computational simulation., Submitted.

[25] P. Perré, I. W. Turner, A 3-D version of TransPore: a comprehensive heat and mass transfer computational model for simulating the drying of

porous media, International Journal of Heat and Mass Transfer 42 (24) (1999) 4501–4521. `doi:10.1016/S0017-9310(99)00098-8`.
URL `http://www.sciencedirect.com/science/article/pii/S0017931099000988`

[26] P. Perré, The Proper Use of Mass Diffusion Equations in Drying Modeling : Introducing the Drying Intensity Number, Drying Technology 33 (15-16) (2015) 1949–1962. `doi:10.1080/07373937.2015.1076836`.
URL `http://dx.doi.org/10.1080/07373937.2015.1076836`

[27] A. Challansonnex, J. Casalinho, P. Perré, Non-Fickian diffusion in bio-based materials : experimental determination of the memory function using minute samples, Submitted.

[28] O. Suchsland, G. E. Woodson, Fiberboard manufacturing Practices In the United States, U.S. Government printing office, 1986.

[29] T. Kawasaki, M. Zhang, S. Kawai, Manufacture and properties of ultra-low-density fiberboard, Journal of wood sciences 44 (1998) 354–360.

[30] Ł. Czajkowski, W. Olek, J. Weres, R. Guzenda, Thermal properties of wood-based panels : specific heat determination, Wood Science and Technology 50 (3) (2016) 537–545. `doi:10.1007/s00226-016-0803-7`.

[31] J. Lux, A. Ahmadi, C. Gobbe, C. Delisée, Macroscopic thermal properties of real fibrous materials : Volume averaging method and 3D image analysis, International Journal of Heat and Mass Transfer 49 (2006) 1958–1973. `doi:10.1016/j.ijheatmasstransfer.2005.09.038`.

[32] O. Vololonirina, M. Coutand, B. Perrin, Characterization of hygrothermal properties of wood-based products - Impact of moisture content and temperature, Construction and Building Materials 63 (2014) 223–233. `doi:10.1016/j.conbuildmat.2014.04.014`.
URL `http://dx.doi.org/10.1016/j.conbuildmat.2014.04.014`

[33] G. Almeida, R. Rémond, P. Perré, Hygroscopic behaviour of lignocellulosic materials: Dataset at oscillating relative humidity variations, Journal of Building Engineering 170 (2018) 716–724.

[34] S. Ganev, R. Beauregard, G. Gendron, Effect of pannel moisture content and density on moisture movement in MDF, Wood and Fiber Science 35 (1) (2003) 68–82.

[35] W. Sonderegger, P. Niemz, Thermal conductivity and water vapour transmission properties of wood-based materials, European Journal of Wood and Wood Products 67 (3) (2009) 313–321. `doi:10.1007/s00107-008-0304-y`. URL `http://link.springer.com/10.1007/s00107-008-0304-y`

[36] X. P. Ye, J. Julson, M. Kuo, A. Womac, D. Myers, Properties of medium density fiberboards made from renewable biomass, Bioresource Technology 98 (5) (2007) 1077–1084. `doi:10.1016/j.biortech.2006.04.022`.

[37] E. Agoua, S. Zohoun, P. Perré, A double climatic chamber used to measure the diffusion coefficient of water in wood in unsteady-state conditions: Determination of the best fitting method by numerical simulation, International Journal of Heat and Mass Transfer 44 (19) (2001) 3731–3744. `doi:10.1016/S0017-9310(01)00022-9`.

[38] R. Byron Bird, W. E. Stewart, E. N. Lightfoot, Transport phenomena, 2nd Edition, John Wiley & Sons, New York, 2002.

[39] P. Perré, A. Challansonnex, J. Colin, On the importance of heat and mass transfer coupling for the characterization of hygroscopic insulation materials, International Journal of Heat and Mass Transfer 133 (2019) 968–975.

[40] W. Ai, H. Duval, F. Pierre, P. Perré, A novel device to measure gaseous permeability over a wide range of pressures: Characterisation of slip flow for Norway spruce, European beech, and wood-based materials, Holzforschung 71 (2) (2016) 147–162.

[41] M. Louërat, M. Ayouz, P. Perré, Heat and moisture diffusion in spruce and wood panels computed from 3-D morphologies using the Lattice Boltzmann method, International Journal of Thermal Sciences 130 (2018) 471–483. `doi:10.1016/j.ijthermalsci.2018.05.009`.
URL `https://doi.org/10.1016/j.ijthermalsci.2018.05.009`

[42] M. Goulet, Phénomènes de second ordre de la sorption d'humidité dans le bois au terme d'un conditionnement de trois mois à température normale. Seconde partie : Essais du bois d'érable à sucre en compression radiale., Note de recherches note de recherche n °3, Université Laval, Québec, Canada (1968).

[43] W. T. Simpson, Moisture changes induced in red oak by transverse stress, Wood and Fiber Science 3 ((1)) (2007) 13–20.

[44] A. Mårtensson, Mechano-sorptive effects in wooden material, Wood Science and Technology 28 (6) (1994) 437–449. `doi:10.1007/BF00225463`.

[45] L. Wadsö, Describing non-Fickian water-vapour sorption in wood, Journal of Materials Science 29 (9) (1994) 2367–2372. `doi:10.1007/BF00363428`.